

Dynamic control of topological phase of Dirac semimetallic terahertz metasurface

Chenglong Wang(王成龙), Zhihua Han(韩志华), Xiang Hou(侯翔), Yansheng Shao(邵延胜), Fangze Deng(邓方泽), Keke Cheng(程可可), Yuchao Li(李玉超), Ke Ma(马克), Yumeng Ma(马宇萌), Huiyun Zhang(张会云), Meng Liu(刘蒙), and Yuping Zhang(张玉萍)

Citation: Chin. Phys. B, 2026, 35 (**3**): 034207. DOI: 10.1088/1674-1056/adfbd8
http://cpb.iphy.ac.cn; http://iopscience.iop.org/cpb

What follows is a list of articles you may be interested in

Transmission property of one-dimensional Dirac-semimetal-defected photonic crystal in terahertz multi-bandgap

Ji-Kai Wang(王济凯), Li Jiang(姜丽), Xue-Fei Yang(杨雪菲), and Ji-He Zhao(赵继和)
Chin. Phys. B, 2026, 35 (**1**): 014209. DOI: 10.1088/1674-1056/ade4b3

Twin pulses of THz generation from a nonlinear crystalline quartz by femtosecond laser pulse

Xiangmei Dong(董祥美), Dan-Ni Li(李丹妮), Zuan-Ming Jin(金钻明), Hui-Ping Zhang(张慧萍), Hong-Guang Li(李宏光), Shao-Hui Wu(吴少晖), Yan Peng(彭滟), Yiming Zhu(朱亦鸣), and Songlin Zhuang(庄松林)
Chin. Phys. B, 2025, 34 (**9**): 094211. DOI: 10.1088/1674-1056/addbcd

Broadband polarization-independent terahertz multifunctional liquid crystal coding metasurface based on topological optimization

Yu Chen(陈羽), Wu-Hao Cao(曹吴昊), Jia-Qi Li(李嘉琦), Ming-Zhe Zhang(张明哲), Xin-Yi Du(杜欣怡), Ding-Shan Gao(郜定山), and Pei-Li Li(李培丽)
Chin. Phys. B, 2025, 34 (**4**): 044205. DOI: 10.1088/1674-1056/adad55

Giant enhancement of negative friction by resonant coupling between localized surface phonon polaritons and graphene plasmonics

Kaipeng Liu(柳开鹏), Shuai Zhou(周帅), Shiwei Dai(戴士为), and Lixin Ge(葛力新)
Chin. Phys. B, 2025, 34 (**1**): 014202. DOI: 10.1088/1674-1056/ad886c

Enhanced picosecond terahertz wave generation based on cascade effects in a terahertz parametric generator

Jingxi Zhang(张敬喜), Yuye Wang(王与烨), Bingfeng Xu(徐炳烽), Kai Chen(陈锴), Zikun Liu(刘紫鲲), Hongru Ma(马鸿儒), Degang Xu(徐德刚), and Jianquan Yao(姚建铨)
Chin. Phys. B, 2024, 33 (**8**): 084203. DOI: 10.1088/1674-1056/ad47b0

Dynamic control of topological phase of Dirac semimetallic terahertz metasurface

Chenglong Wang(王成龙), Zhihua Han(韩志华), Xiang Hou(侯翔), Yansheng Shao(邵延胜), Fangze Deng(邓方泽), Keke Cheng(程可可), Yuchao Li(李玉超), Ke Ma(马克), Yumeng Ma(马宇萌), Huiyun Zhang(张会云), Meng Liu(刘蒙)[†], and Yuping Zhang(张玉萍)[‡]

Qingdao Key Laboratory of Terahertz Technology, College of Electronic and Information Engineering, Shandong University of Science and Technology, Qingdao 266590, *China*

(Received 15 July 2025; revised manuscript received 11 August 2025; accepted manuscript online 15 August 2025)

With the rapid advancement of terahertz technology, multifunctional coding metasurfaces have emerged as a significant research frontier in this domain. However, the rigid geometric structure of traditional metasurfaces poses challenges in accommodating both multifunctionality and dynamic control requirements. This study proposes an adjustable exceptional topological phase coding metasurface device based on a Dirac semimetal (DSM). By optimizing the structural parameters to excite multiple exceptional points (EPs), the resulting topological phase distribution enables multi-dimensional control of terahertz waves. The results demonstrate that, under the incidence of left-handed circularly polarized (LCP) light, the metasurface device can stably generate vortex light with a topological charge of $l = 1$. In the left- and right-handed circularly polarized channels, the wavefronts of the vortex beam and the split beam are independently controlled, enabling dual-channel digital holographic imaging of the numerals '0' and '5'. Near-field grayscale imaging of the 'little grey dog' pattern is achieved by exploiting the differentiated absorption characteristics of the EP under LCP illumination. Furthermore, by dynamically tuning the Fermi level of the DSM, reversible switching of the reflection mode state is realized under the same incident conditions. This research provides a theoretical and practical foundation for enhancing the capacity of terahertz communication systems and optimizing terahertz near-field and far-field imaging technologies. It also holds significant scientific value and application potential for advancing the development of independently adjustable multifunctional devices.

Keywords: terahertz, topological phase, dynamic control, exceptional points

PACS: 42.68.Mj, 81.05.Xj, 42.25.Ja, 78.67.Pt

DOI: 10.1088/1674-1056/adfbd8 **CSTR:** 32038.14.CPB.adfbd8

1. Introduction

Metamaterials are a class of composite materials characterized by artificially designed microstructures, which place them at the forefront of academic and industrial research due to their extraordinary electromagnetic properties.[1] Their two-dimensional variant, known as metasurfaces, enables flexible control over the phase, amplitude, and polarization state of electromagnetic waves by precisely manipulating unit geometry, size parameters, and array arrangement.[2,3] These structures demonstrate exceptional control capabilities across a wide frequency range, from microwave to terahertz and even into the visible spectrum.[4,5] They have been extensively applied in various fields, including beam shaping,[6,7] polarization conversion,[8] holographic imaging,[9] and perfect absorption.[10] Notably, in the terahertz frequency band, metasurfaces provide a platform for the development of low-loss and high-sensitivity devices with subwavelength thickness, significantly mitigating the issues of excessive size and scattering loss commonly associated with traditional bulk materials at longer wavelengths. This advancement injects new impetus into numerous applications, such as high-speed wireless communications, spectral imaging, and advanced optoelectronic technologies.[11] In 2014, Cui *et al.*[12] introduced the innovative concept of employing digital coding to characterize metasurface units, integrating switching diodes within these units to realize the world's first metasurface with real-time programmable functions. This breakthrough enabled metasurfaces to be dynamically reconfigured for the first time. This pioneering achievement has inspired the academic community to extensively explore programmable metasurfaces and digital coding technologies.[13–21] It has also led to the development of coding theory systems, including the addition theorem,[22] the convolution theorem,[23] and logical coding,[24] thereby promoting the theoretical construction and functional expansion of programmable metasurfaces. In the aforementioned research stages, the electromagnetic control of metasurfaces primarily relies on the propagation phase and the Pancharatnam–Berry (PB) phase.[25] In 2021, Song *et al.*[26] first introduced the topological properties of singular points in non-Hermitian systems into optical phase control. By utilizing the unique phase accumulation effect in the exceptional points (EP) neighborhood,[27] they constructed an

[†]Corresponding author. E-mail: liumeng@sdust.edu.cn

[‡]Corresponding author. E-mail: sdust_thz@163.com

© 2026 Chinese Physical Society and IOP Publishing Ltd. All rights, including for text and data mining, AI training, and similar technologies, are reserved.

exceptional topological phase (ETP) and realized an independently controllable metasurface for circularly polarized cross-channels.[26] Subsequent studies further integrated ETP with PB to achieve independent and precise control over dual polarization channels,[28–32] significantly expanding the degrees of freedom in optical phase engineering. These investigations primarily focused on the visible spectrum, benefiting from a broader array of tunable nanomaterials and mature lithographic processes, achieving phase control capabilities as high as 2π or beyond. In 2025, Lang *et al.*[33] experimentally explored ETP in the terahertz regime for the first time, designing a spin-decoupled surface plasmon device with wavefront manipulation capabilities. In the same year, Kim *et al.*[34] realized the first tunable ETP metasurface in the visible range, utilizing electrically active metasurfaces based on conductive polymers operating under low voltage, thereby enabling control over unique topological phases.

Although preliminary efforts have extended ETP theory into the terahertz domain, current terahertz ETP metasurfaces still encounter several distinct challenges, including the scarcity of low-loss materials,[35] fabrication difficulties at subwavelength precision, and integration issues of microdiodes due to size constraints, which hinder the realization of dynamic tunability. Nevertheless, the introduction of phase-change materials and tunable materials offers a promising avenue to address these limitations.[36] By applying external stimuli such as voltage, temperature, and light intensity,[37] metasurfaces can transition between different states to achieve the desired tuning effects. DSMs, characterized by high carrier mobility, ease of fabrication, and excellent chemical stability,[38,39] not only provide a robust material foundation for dynamic response in the terahertz range but also demonstrate superior continuous tunability near EP regimes in optical responses.[40] Compared to two-dimensional materials such as graphene, DSMs exhibit enhanced thermal stability and greater design flexibility for device architectures, making them well-suited for the construction of complex, multifunctional ETP devices.

This study proposes a terahertz-tunable ETP coding metasurface based on a three-dimensional DSM. By constructing a parity-time (PT) symmetric structure, it is observed that the polarization eigenstate becomes degenerate at the EP, and the significant phase accumulation effect around the EP can be utilized for multifunctional regulation. The results indicate that by adjusting the DSM Fermi level, dynamic switching of the circularly polarized terahertz wave reflection characteristics can be achieved while maintaining the same metasurface structure. Under LCP incidence, ETPs with topological charges of $+1$ and -1 are simultaneously observed within the same parameter space, thus satisfying the conservation of topological charge in the Brillouin zone. The switching control of the vortex beam is realized through ETP coding in the conversion channel from LCP to right-handed circularly polarized (RCP) light. When RCP is incident, a third EP, independent of the LCP channel, along with its phase accumulation phenomenon, can be detected. Furthermore, by integrating the PB phase, independent regulation and switching functions of holographic imaging and beam shaping for the two polarization channels are achieved. Additionally, the three EPs coexist at the same frequency, revealing significant differences in the absorption characteristics of LCP and RCP, with these differences becoming more pronounced upon rotation of the structure. Leveraging this characteristic, the on-off switching function for grayscale imaging of the 'little grey dog' was successfully realized. This research provides a novel theoretical and technical pathway for the advancement of terahertz high-capacity communication systems, controllable near-field imaging, and holographic technology.

2. Theory and methods

2.1. Coupled-mode theory

In this study, coupled-mode theory is employed to analyze the reflection characteristics of DSM-coded metasurfaces in the terahertz band. We assume that the incident electric field is given by $E_i = \boldsymbol{E}_i\, \mathrm{e}^{\mathrm{i}\omega t}$, where $\boldsymbol{E}_i = \begin{pmatrix} E_{ix} \\ E_{iy} \end{pmatrix}$. The corresponding effective dipole moment is expressed as $p_{x,y} = \boldsymbol{p}_{x,y}\, \mathrm{e}^{\mathrm{i}\omega t}$, and the radiation coupling intensity between the two is g_j. The resonant frequency is denoted as ω_0, and the damping coefficient is represented by γ, which describes the rate of energy dissipation when the system vibrates. When the incident frequency is close to the resonance ($\sigma = \omega - \omega_0 \approx 0$) and the damping is much smaller than the resonance frequency ($\gamma \ll \omega_0$), the relationship between the dipole moment and the incident electric field satisfies the polarizability matrix equation[41]

$$\left[\begin{pmatrix} \sigma_x + \mathrm{i}\gamma_x & 0 \\ 0 & \sigma_y + \mathrm{i}\gamma_y \end{pmatrix} + \begin{pmatrix} G_{xx} & G_{xy} \\ G_{yx} & G_{yy} \end{pmatrix}\right] \begin{pmatrix} p_x \\ p_y \end{pmatrix} = \begin{pmatrix} g_x E_{ix} \\ g_y E_{iy} \end{pmatrix}, \tag{1}$$

Among them, γ_y and γ_x respectively represent the damping magnitudes in the y and x directions, and G_{ik} characterizes the radiation field coupling term generated in the i direction by the dipole moment in the k direction. For a square lattice, $G_{xx} = G_{yy}$, and reciprocity requires $G_{xy} = G_{yx}$. The reflected field can be obtained by superimposing the incident field reflected from the ground mirror and the field radiated in the forward direction by the oscillating dipole, which is given by $\frac{\mathrm{i}\omega\eta_0}{2\alpha^2}\begin{pmatrix} g_x p_x \\ g_y p_y \end{pmatrix}$, where $\eta_0 = \sqrt{\mu_0/\varepsilon_0}$ is the free-space impedance and A is the lattice constant[26]

$$\begin{pmatrix} E_{rx} \\ E_{ry} \end{pmatrix} = \boldsymbol{r}\begin{pmatrix} E_{ix} \\ E_{iy} \end{pmatrix} = \frac{\mathrm{i}\omega\eta_0}{2\alpha^2}\begin{pmatrix} p_x \\ p_y \end{pmatrix} - \begin{pmatrix} E_{ix} \\ E_{iy} \end{pmatrix}, \tag{2}$$

The passive system can be divided into an anisotropic PT-symmetric part and an isotropic lossy part[27]

$$\begin{pmatrix} -\mathrm{i}\Gamma & G_{xy} \\ G_{xy} & \mathrm{i}\Gamma \end{pmatrix}\begin{pmatrix} p_x \\ p_y \end{pmatrix} + S\begin{pmatrix} p_x \\ p_y \end{pmatrix} = \begin{pmatrix} g_x E_{ix} \\ g_y E_{iy} \end{pmatrix}, \tag{3}$$

where $S=\sigma+G_{xx}+\mathrm{i}(\gamma_y+\gamma_x)/2$ and $\Gamma=(\gamma_y-\gamma_x)/2$. Equation (3) describes the oscillator model with balanced loss and gain and the background medium with identical loss. The first matrix satisfies PT symmetry, implying that the system can reach PT symmetry and EP conditions, whereas the unit matrix in the second term only shifts the eigenvalues without affecting the polarization eigenstates. $\overleftrightarrow{I}$ is the identity matrix. Equation (2) can therefore be rewritten as

$$\begin{pmatrix} E_{rx} \\ E_{ry} \end{pmatrix} = \left[C\begin{pmatrix} g_x^2(\sigma_y+\mathrm{i}\gamma_y+G_{yy}) & -g_x g_y G_{xy} \\ -g_x g_y G_{xy} & g_y^2(\sigma_x+\mathrm{i}\gamma_x+G_{xx}) \end{pmatrix} - \overleftrightarrow{I} \right]\begin{pmatrix} E_{ix} \\ E_{iy} \end{pmatrix}, \tag{4}$$

where

$$C=\frac{\mathrm{i}\omega\eta_0}{2\alpha^2\left[(\sigma_x+\mathrm{i}\gamma_x+G_{xx})(\sigma_y+\mathrm{i}\gamma_y+G_{yy})-G_{xy}^2\right]}.$$

Combined with the above equations, the reflection matrix can be simplified to

$$\begin{aligned}\begin{pmatrix} E_{rx} \\ E_{ry} \end{pmatrix} &= \left[g_x g_y C\begin{pmatrix} -\mathrm{i}\Gamma & G_{xy} \\ G_{xy} & \mathrm{i}\Gamma \end{pmatrix}\right]\begin{pmatrix} E_{ix} \\ E_{iy} \end{pmatrix} \\ &\quad + (g_x g_y CS-1)\overleftrightarrow{I}\begin{pmatrix} E_{ix} \\ E_{iy} \end{pmatrix},\end{aligned} \tag{5}$$

Since the reflection matrix has the same eigenstates as $\begin{pmatrix} -\mathrm{i}\Gamma & G_{xy} \\ G_{xy} & \mathrm{i}\Gamma \end{pmatrix}$, its eigenvalues reveal the EP and PT symmetries of the system.

2.2. Pancharatnam–Berry phase

To construct the topological phase control mechanism, we further introduce PB phase theory. When the rotation angle of the metasurface structure relative to the reference coordinate system is denoted as θ, the circular polarization reflection matrix can be expressed as[32]

$$\boldsymbol{r}^{\theta}(R)=\begin{pmatrix} r_{++}^{\theta}(R) & r_{+-}^{\theta}(R) \\ r_{-+}^{\theta}(R) & r_{--}^{\theta}(R) \end{pmatrix} = M(-\theta)\boldsymbol{r}(R)M(\theta), \tag{6}$$

Using the Pauli matrices $\{\delta_1,\delta_2,\delta_3\}$, the matrix $M=\mathrm{e}^{\mathrm{i}\theta\delta_3}$ can be expanded as $M(\theta)=\cos\theta+\mathrm{i}\sin\theta\sigma_3$. The reflection matrix can be further expanded as

$$\begin{aligned}\boldsymbol{r}^{\theta}(R) &= \frac{1}{2}(r_{xx}+r_{yy})+\frac{\mathrm{i}}{2}(r_{xy}-r_{yx})\delta_3 \\ &\quad +\frac{1}{2}(r_{xx}-r_{yy})\left(\mathrm{e}^{-\mathrm{i}2\theta}\delta_+ + \mathrm{e}^{\mathrm{i}2\theta}\delta_-\right) \\ &\quad +\frac{\mathrm{i}}{2}(r_{xy}+r_{yx})\left(-\mathrm{e}^{-\mathrm{i}2\theta}\delta_+ + \mathrm{e}^{\mathrm{i}2\theta}\delta_-\right),\end{aligned} \tag{7}$$

where r_{xy} represents polarization conversion from a y-polarized incident wave to an x-polarized reflected wave, and $+$ and $-$ represent LCP and RCP, respectively. Therefore, the cross-polarized reflection r_{-+}^{θ} can be expressed as a composite formula describing the original phase and the rotation angle

$$r_{-+}^{\theta}(R)=\frac{(r_{xx}-r_{yy})+\mathrm{i}(r_{xy}+r_{yx})}{2}\mathrm{e}^{\mathrm{i}2\theta}=r_{-+}^{0}(R)\mathrm{e}^{\mathrm{i}2\theta}, \tag{8}$$

where r_{-+}^{0} represents the phase of the original structure without rotation. When the unit structure is rotated by θ, a geometric phase of -2θ is added to r_{+-}, and the circular polarization conversion formula can be written as

$$\begin{aligned}r_{+-}^{\theta}(R) &= \frac{(r_{xx}-r_{yy})-\mathrm{i}(r_{xy}+r_{yx})}{2}\mathrm{e}^{-\mathrm{i}2\theta} \\ &= r_{-+}^{0}(R)\mathrm{e}^{-\mathrm{i}2\theta},\end{aligned} \tag{9}$$

The coupled-mode theory presented herein elucidates the conditions and reflection characteristics of EP generation on PT-symmetric metasurfaces, while PB phase analysis provides the geometric phase contribution of unit rotation to circular polarization channels. Collectively, these elements establish a robust theoretical foundation for achieving terahertz-tunable exceptional topological phase coding based on three-dimensional DSM in this paper.

3. Results and discussion

3.1. The principle and meta-atoms design

The DSM terahertz metasurface unit cell designed in this work is illustrated in Fig. 1. It comprises three layers arranged from bottom to top: the bottom layer is an aluminum (Al) reflector that enables total reflection; the middle layer is a silica (SiO_2) dielectric spacer; and the top layer consists of a chiral structure composed of L-shaped and linear DSM elements arranged in a two-dimensional array. In this paper, CST Microwave Studio is employed for numerical simulations. Periodic boundary conditions are applied in the x and y directions, while open boundary conditions are applied along the z direction. The complex conductivity of the DSM is calculated using the Kubo formula within the random phase approximation (RPA) framework. In the low-temperature limit $T \ll E_{\mathrm{F}}$, it can be expressed as[42]

$$\mathrm{Re}\left(\sigma(\Omega)\right)=\frac{e^2}{h}\frac{gK_{\mathrm{F}}}{24\pi}\Omega G(\Omega-2), \tag{10}$$

$$\mathrm{Im}\left(\sigma(\Omega)\right)=\frac{e^2}{h}\frac{gK_{\mathrm{F}}}{24\pi}\left[\frac{4}{\Omega}-\ln\left(\frac{4\varepsilon_{\mathrm{c}}}{|\Omega^2-4|}\right)\right], \tag{11}$$

where e is the elementary charge, h is Planck's constant, $K_{\mathrm{F}}=E_{\mathrm{F}}/(h v_{\mathrm{F}})$ is the Fermi momentum, G is the unit step function, $\Omega=h\omega/E_{\mathrm{F}}+\mathrm{i}h\tau^{-1}/E_{\mathrm{F}}$, $v_{\mathrm{F}}=1\times10^6\ \mathrm{m\cdot s^{-1}}$ is the Fermi velocity, E_{F} is the Fermi level, $\tau=\mu E_{\mathrm{F}}/(e v_{\mathrm{F}}^2)$ is the relaxation time, and $\mu=3\times10^4\ \mathrm{cm^2\cdot V^{-1}\cdot s^{-1}}$. Here, $\varepsilon_{\mathrm{c}}=E_{\mathrm{c}}/E_{\mathrm{F}}$, where E_{c} is the cutoff energy. In this work, AlCuFe quasicrystal is selected as the DSM, and the degeneracy factor $g=40$ is

adopted. The complex relative dielectric constant of the DSM is expressed as[6]

$$\varepsilon = \varepsilon_b + \frac{\mathrm{i}\delta}{\omega\varepsilon_0}, \tag{12}$$

where $\varepsilon_b = 1$ and ε_0 is the vacuum permittivity. The presence of the metal ground plane completely suppresses transmission.

The resonant response of the chiral structure can be excited by both x- and y-polarized incident waves. Figure 2(a) shows the simulated reflection spectra when L_3 is fixed at 7 μm while L_1 varies from 1 μm to 4 μm. Since the effective length of the DSM chiral structure in the x direction is insensitive to variations in L_3, the resonance frequency of the x-polarized reflection coefficient r_{xx} remains nearly unchanged. In contrast, the effective length in the y direction increases with L_1, so the y-direction resonance is primarily governed by L_1. Consequently, the resonance position of the y-polarized reflection coefficient r_{yy} shifts with increasing L_1, accompanied by a reduction in resonance strength. Figure 2(b) presents the simulation results with L_1 fixed at 4 μm while L_3 increases from 6.5 μm to 9.5 μm. In this case, the effective length in the y direction remains nearly constant, resulting in an almost unchanged r_{yy} resonance, whereas the increase in the effective length in the x direction induces a pronounced frequency shift in the r_{xx} resonance. Therefore, by jointly tuning L_1 and L_3, controllable crossover of resonance frequencies in orthogonal polarization channels can be achieved, enabling the two modes to approach degeneracy in parameter space and indicating the potential emergence of EPs.

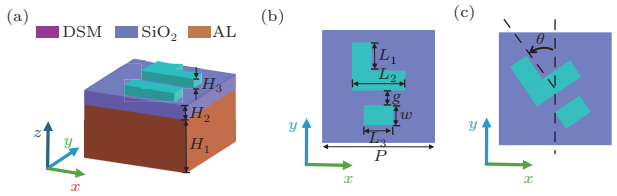


Fig. 1. Schematic diagram of a DSM metasurface unit. (a) The thicknesses of the three layers from bottom to top are $H_1 = 15$ μm, $H_2 = 4$ μm, and $H_3 = 3$ μm. (b) The lattice period is $p = 30$ μm, with a gap $g = 7$ μm and structure width $w = 5$ μm. The geometric parameters are $L_1 = 5.8$ μm, $L_2 = 14$ μm, and $L_3 = 7.6$ μm. (c) θ denotes the rotation angle around the center of the structure.

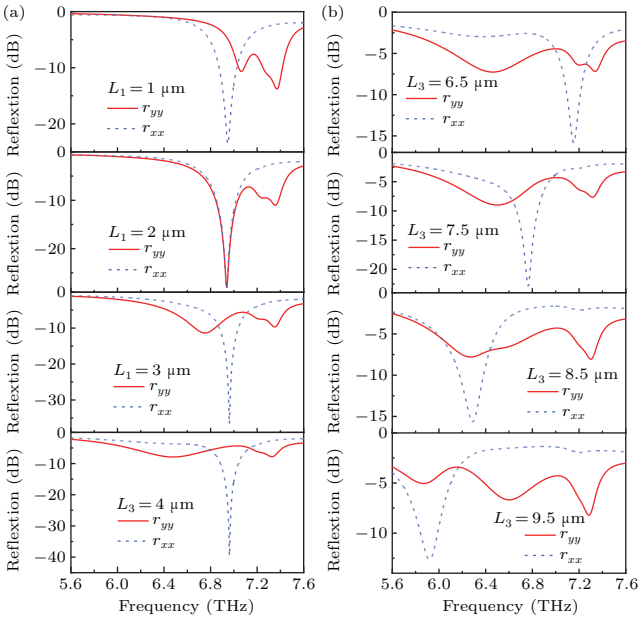


Fig. 2. (a) Simulated reflection coefficients r_{yy} and r_{xx} of the DSM metasurface as L_1 increases, with $L_3 = 7$ μm. (b) Simulated reflection coefficients r_{yy} and r_{xx} of the DSM metasurface as L_3 increases, with $L_1 = 4$ μm.

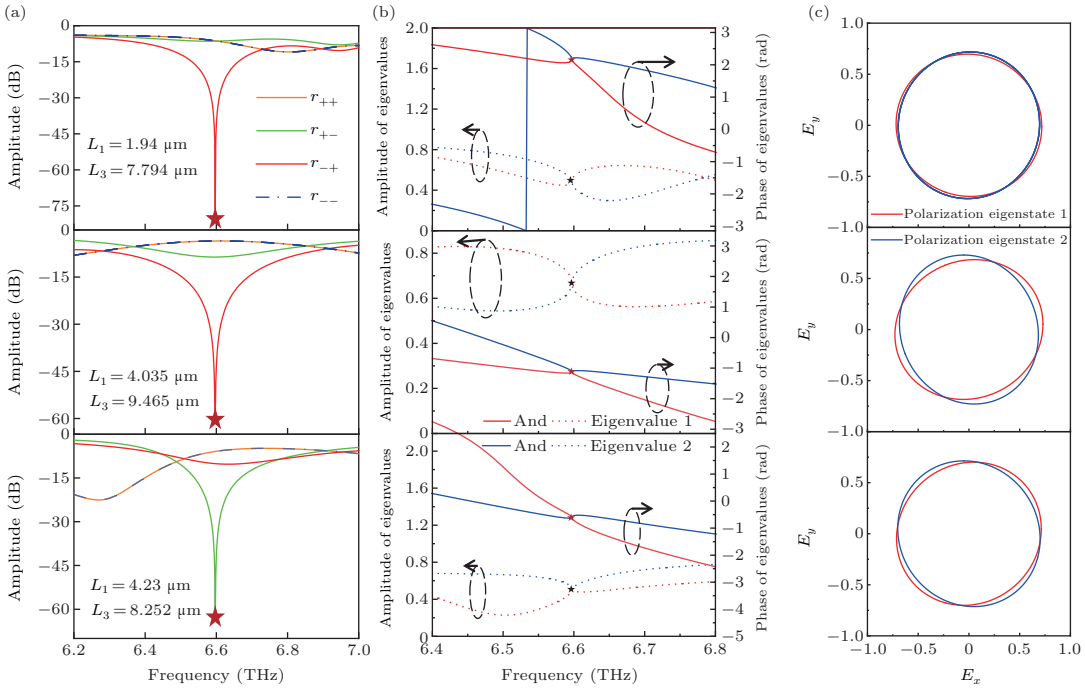


Fig. 3. (a) Reflection spectra, (b) amplitude and phase of the eigenvalues, and (c) eigenstates of the chiral unit structures with parameters (L_1, L_3) of the DSM metasurface at (1.94 μm, 7.794 μm), (4.035 μm, 9.465 μm), and (4.23 μm, 8.252 μm), respectively.

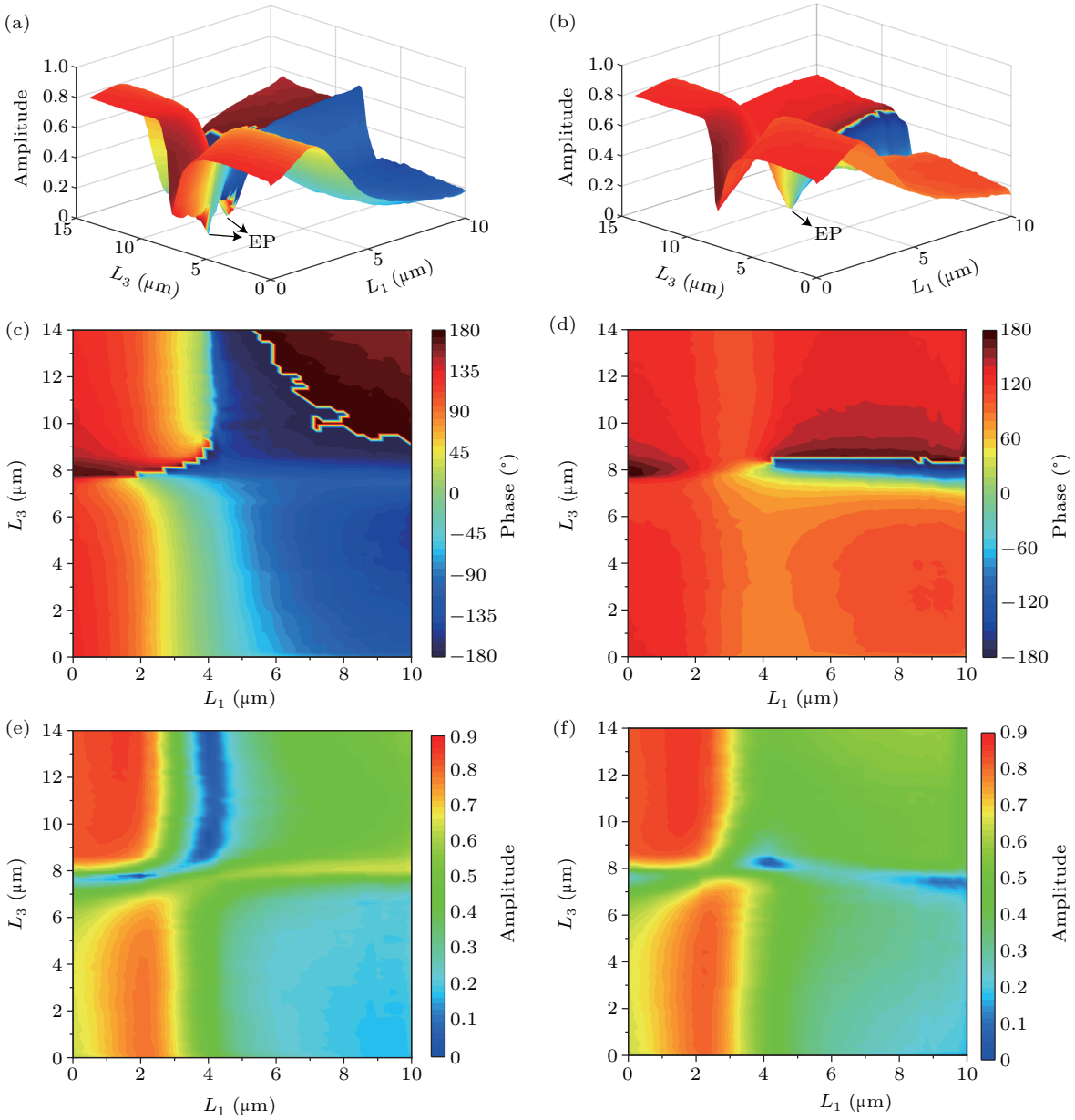


Fig. 4. In the range of $L_1 \in [0, 10]$ μm and $L_3 \in [0, 14]$ μm, the (a) three-dimensional parameter space distribution, (c) two-dimensional parameter space phase distribution, and (e) two-dimensional parameter space amplitude distribution of the DSM metasurface r_{-+}; the (b) three-dimensional parameter space distribution, (d) two-dimensional parameter space phase distribution, and (f) two-dimensional parameter space amplitude distribution of the DSM metasurface r_{+-}.

Additionally, the chiral response of the metasurface is fully characterized by the reflection scattering matrix

$$\boldsymbol{r} = \begin{pmatrix} r_{++} & r_{+-} \\ r_{-+} & r_{--} \end{pmatrix}, \tag{13}$$

where r_{-+} denotes the reflection coefficient for an LCP incident wave converted to RCP, and r_{+-} denotes the reflection coefficient for an RCP incident wave converted to LCP. r_{++} and r_{--} correspond to co-polarized reflections for LCP and RCP incidence, respectively. From the reflection matrix, it follows that $r_{++} = r_{--}$, and the eigenvalues are given by $r_{1,2} = r_{++} \pm \sqrt{r_{+-} r_{-+}}$. When $r_{+-} r_{-+} = 0$, the two eigenvalues become degenerate, indicating the occurrence of an EP in the system.

When the DSM Fermi level is set to 0.5 eV, the unit-cell structural parameters (L_1, L_3) are tuned, and both LCP and RCP incidences are considered. As a result, three EPs are simultaneously obtained at 6.597 THz. Under LCP incidence, EPs with topological charges of -1 and $+1$ are generated at (1.94 μm, 7.794 μm) and (4.035 μm, 9.465 μm), respectively. Conversely, under RCP incidence, an EP with a topological charge of -1 is generated at (4.23 μm, 8.252 μm). The reflection spectra indicate that the conversion channels from LCP to RCP and from RCP to LCP disappear under LCP and RCP incidences, respectively, which is one of the key signatures of the emergence of EPs, as shown in Fig. 3(a). Furthermore, by incorporating the incident conditions of linearly polarized light in the x and y directions, an equivalent 2×2 non-Hermitian

metasurface reflection matrix is constructed, and its eigenspectrum in the frequency domain is analyzed. It is demonstrated that both the eigenvalues and eigenstates are degenerate at the aforementioned frequency points (Figs. 3(b) and 3(c)), further substantiating the existence of EPs.

In addition, by scanning the (L_1, L_3) parameter space at a fixed frequency of 6.597 THz, it was observed that at (1.94 μm, 7.794 μm), the LCP-to-RCP channel disappeared, forming an EP with a topological charge of -1, surrounded by a phase accumulation of -2π; continuing to adjust to (4.035 μm, 9.465 μm), an EP with a topological charge of $+1$ appeared, exhibiting a phase accumulation of $+2\pi$. As shown in Fig. 4(a), the two EPs coexist in the same parameter space, demonstrating the topological conservation property that EPs with topological charges of ±1 appear in pairs in the Brillouin zone. Further adjusting the (L_1, L_3) parameters, a third EP occurs at (4.23 μm, 8.252 μm), which is characterized by the disappearance of the RCP-to-LCP channel, a topological charge of -1, and a phase accumulation of -2π, as illustrated in Fig. 4(b). The phase and amplitude corresponding to the two channels are depicted in Figs. 4(c)–4(f). Specifically, Figs. 4(c) and 4(d) present the phase distribution of the r_{-+} and r_{+-} channels within the (L_1, L_3) parameter space. It is evident that the phase at the EP exhibits a $\pm2\pi$ jump, resulting in a typical phase winding structure. Figures 4(e) and 4(f) illustrate the two-dimensional distribution of the reflection amplitude of the channels, indicating a significant reduction in reflection intensity around the EP, which approaches zero. This observation confirms the complete disappearance of the reflection channel at the EP. Collectively, these features provide direct physical evidence of the EP.

3.2. Control of vortex beam switching based on singular topological phase

Building upon the EP characteristics discussed above, we found that under LCP incidence, by adjusting the structural parameters (L_1, L_3), the 2π phase accumulation required for surrounding coding, i.e., the ETP, can be established around the EP. Four groups of structural units were selected to satisfy a $\pi/2$ discrete phase difference at a frequency of 6.597 THz, while maintaining consistent reflection amplitudes (approximately 0.45) when the DSM Fermi level is set at 0.5 eV. The corresponding parameters (L_1, L_3) are (7.8 μm, 12.2 μm), (1.2 μm, 7.2 μm), (4 μm, 1.6 μm), and (5.8 μm, 7.6 μm) (see Fig. 5(a)).

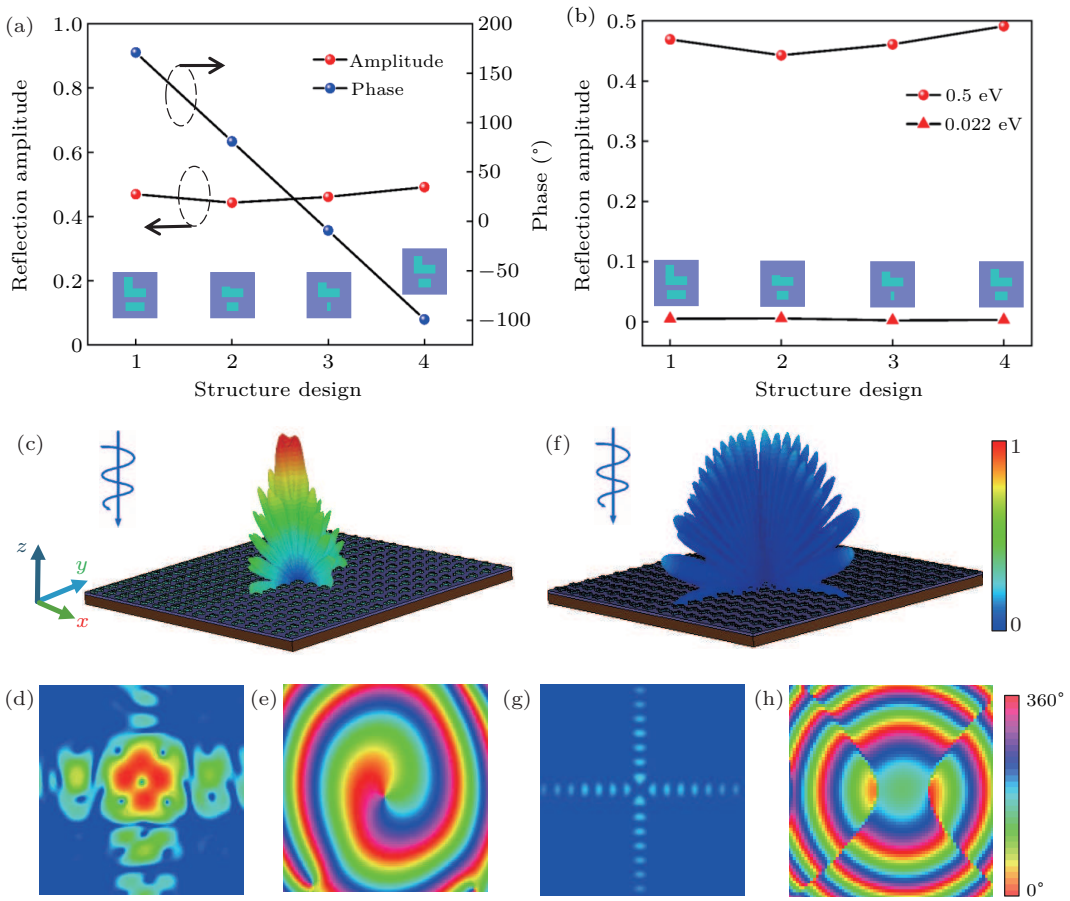


Fig. 5. Reflection and vortex characteristics of the DSM metasurface under LCP incidence at 6.597 THz. (a) Cross-polarization reflection amplitude and phase distribution for four structural units when the DSM Fermi level is $E_F = 0.5$ eV. (b) Comparison of cross-polarization reflection amplitudes at high ($E_F = 0.5$ eV) and low ($E_F = 0.022$ eV) Fermi levels. Reflected light field characteristics when the vortex beam is on at $E_F = 0.5$ eV: (c) three-dimensional intensity distribution, (d) amplitude, and (e) phase. Reflected light field characteristics when the vortex beam is off at $E_F = 0.022$ eV: (f) three-dimensional intensity distribution, (g) amplitude, and (h) phase.

As illustrated in Fig. 5(b), when the DSM Fermi level is lowered to 0.022 eV, the reflection amplitudes of all four units approach zero, achieving high-contrast switching behavior. Based on the phase distribution law of vortex light generated by the metasurface,

$$\Delta\varphi = \frac{2\pi l}{2^n}.$$

Ref. [43], arranging the structural units according to a 45° phase gradient, enables the generation of a vortex beam with topological charge $l = 1$ using a 32×32 metasurface array at 6.597 THz.

Figures 5(c)–5(e) demonstrate that at a high Fermi level ($E_F = 0.5$ eV), the metasurface stably produces distinct amplitude and spiral phase patterns. Conversely, at a low Fermi level ($E_F = 0.022$ eV), the vortex beam is completely suppressed, resulting in a nearly negligible reflection signal (Figs. 5(f)–5(h)). These results demonstrate that the integration of ETP with tunable DSM materials enables efficient switching control of vortex beams, providing a compact and effective approach for vortex optical communication and dynamic mode multiplexing.

3.3. Dual-channel beam control and holographic imaging of LCP and RCP

Compared to conventional metasurfaces, ETP coding metasurfaces offer enhanced flexibility and functional integration in the manipulation of circularly polarized light. Here, we investigate the independent real-time control of dual-channel metasurfaces under LCP and RCP incidences. By leveraging the highly sensitive phase response introduced by ETP in the conversion channel containing the EP, together with the relatively flat phase background in the non-working channel, ETP is combined with the PB phase mechanism to realize complex phase encoding for dual-channel multiplexing.

Specifically, under LCP incidence, two structural units exhibiting a 180° phase difference at a DSM Fermi level of $E_F = 0.5$ eV are selected. Their respective dimensions, (L_1, L_3), are (3.4 μm, 9.4 μm) and (7.2 μm, 3.8 μm), serving as the "0" and "1" units for phase encoding (see Fig. 6). By further rotating these two structures counterclockwise by 90°, a 180° phase difference can be generated in the RCP channel via the PB phase principle, thereby establishing a dual-channel coding system.

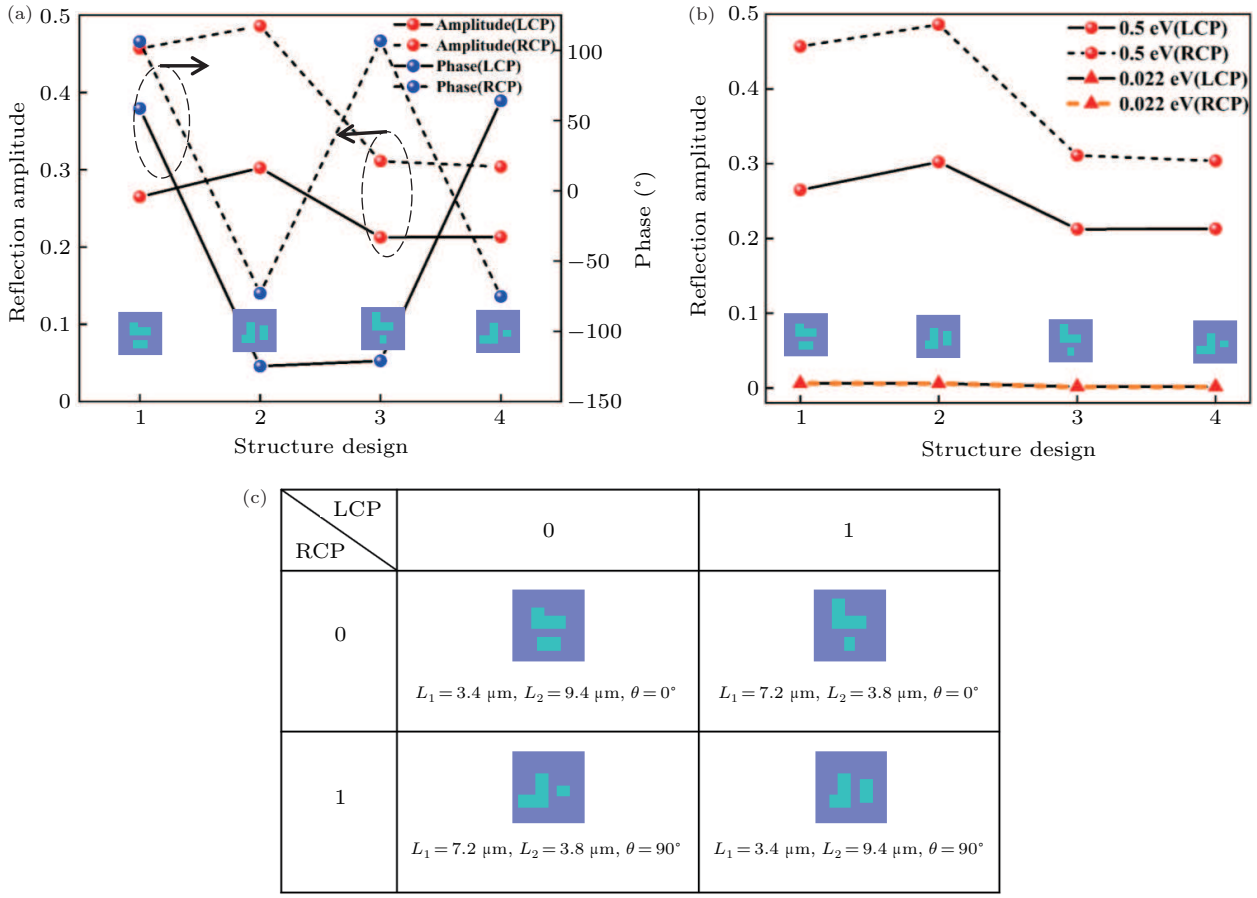


Fig. 6. Dual-channel circular polarization control and coding of the DSM metasurface at 6.597 THz. (a) Reflection amplitude and phase of the four structural units under LCP and RCP incidences at $E_F = 0.5$ eV. (b) Comparison of reflection amplitudes of the four units at $E_F = 0.5$ eV and $E_F = 0.022$ eV, showing 'on' and 'off' states. (c) Phase coding states and geometric parameters of the four units under LCP and RCP channels, indicating the dual-channel '0' and '1' coding logic.

Figure 6(a) shows the reflection phase and amplitude distribution of the four units under LCP and RCP incidences at $E_F = 0.5$ eV. Figure 6(b) presents the reflection amplitude variation at different Fermi levels. At $E_F = 0.022$ eV, the reflections of all four metasurface units for both LCP and RCP light approach zero, confirming the 'off state' under low Fermi level conditions. Figure 6(c) depicts the phase coding states and geometric parameters of the units in a matrix format, with rows and columns corresponding to RCP and LCP channel coding, respectively. The structural dimensions and rotation angles of each unit are indicated, clearly illustrating the dual-channel phase control logic for "0" and "1" coding.

A 32×32 metasurface array is designed to achieve programmable phase control across both channels. To reduce coupling between adjacent units, each structural unit comprises a 3×3 sub-unit configuration. Under LCP incidence, the metasurface can generate vortex beams with varying topological charge l and deflection angle θ_r. The required reflection phase distribution is given by

$$\varphi(x,y) = l \cdot \arctan\left(\frac{y}{x}\right) + k_0 \cdot x \sin\theta_r, \tag{14}$$

where (x,y) denotes the coordinate position on the metasurface, and k_0 is the free-space wave number.

Based on this phase distribution, the constructed metasurface vortex phase arrangement is illustrated in Fig. 7(a).

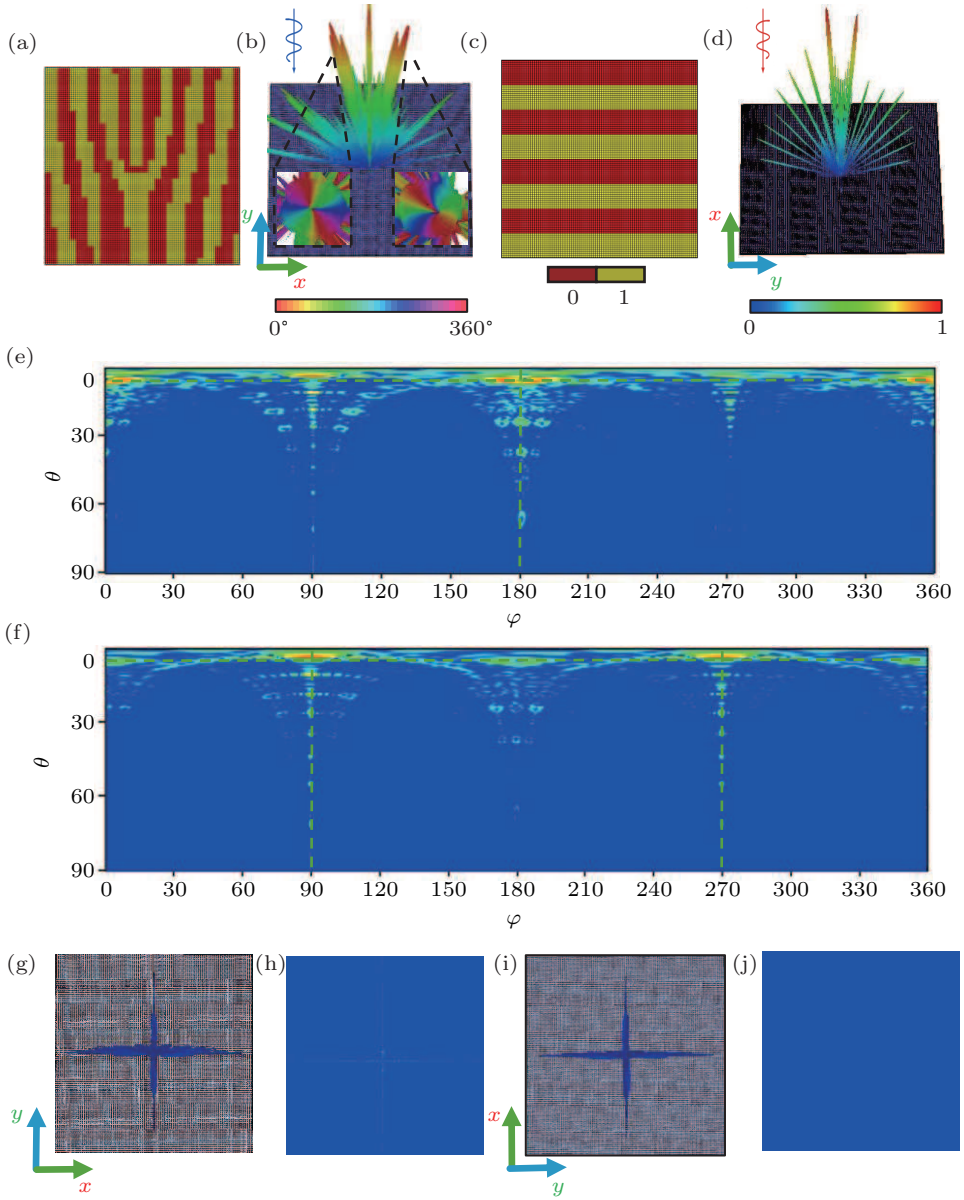


Fig. 7. Wavefront control characteristics of the DSM metasurface under LCP and RCP incidence at a frequency of 6.597 THz. The metasurface phase arrangement shows (a) the vortex phase distribution under LCP incidence and (c) the light beam splitting phase distribution. The reflected light field characteristics of the vortex light under LCP incidence when DSM $E_F = 0.5$ eV include: (b) three-dimensional intensity distribution and (e) amplitude. The reflected light field characteristics of the vortex light turned off when DSM $E_F = 0.022$ eV include: (g) three-dimensional intensity distribution and (h) amplitude. The reflected light field characteristics of the light beam splitting under RCP incidence when DSM $E_F = 0.5$ eV include: (d) three-dimensional intensity distribution and (f) amplitude. The reflected light field characteristics of the light beam splitting turned off when DSM $E_F = 0.022$ eV include: (i) three-dimensional intensity distribution and (j) amplitude.

Additionally, under RCP incidence, the metasurface structure can achieve a beam-splitting function, with the corresponding reflection phase distribution described by the following formula:[13]

$$k_0 \sin\theta_r = k_0 \sin\theta_i + \frac{d\varphi}{dx}, \tag{15}$$

where θ_i is the incident angle and dx is the spatial period of the same reflection phase unit. The beam-splitting phase calculated using this expression is illustrated in Fig. 7(c).

Based on the configurations of the two aforementioned phase plates, the metasurface is systematically arranged. According to the distinct coding phases provided by the coding units under dual channels, as depicted in Fig. 7, the metasurface phase plate is organized accordingly.

Under LCP incidence, a double vortex beam splitting with topological charges of $+2$ and -2 is generated, resulting in deflection angles (φ, θ_r) of approximately (0°, 3.62°) and (180°, 3.62°) in the x-direction. Conversely, under RCP incidence, beam splitting occurs in the y-direction, with deflection angles (φ, θ_r) of approximately (90°, 3.62°) and (270°, 3.62°).

As illustrated in Figs. 7(b), 7(d), 7(e), and 7(f), when the DSM Fermi level is set to 0.5 eV, the metasurface effectively facilitates wavefront control.

Furthermore, upon adjusting the DSM Fermi level to 0.022 eV, the reflection from the test metasurface unit approaches zero, resulting in neither LCP nor RCP incident waves producing effective reflection output, as depicted in Figs. 7(g)–7(j). This demonstrates that the constructed metasurface can achieve independent regulation and high-contrast optical switching across LCP and RCP channels.

To further verify the independent controllability of the LCP and RCP dual channels, we employed the iterative Fourier transform-Gerchberg–Saxton (GS) algorithm to extract the phase distribution of the target images labeled '0' and '5'.[44] The results are illustrated in Figs. 8(a)–8(d).

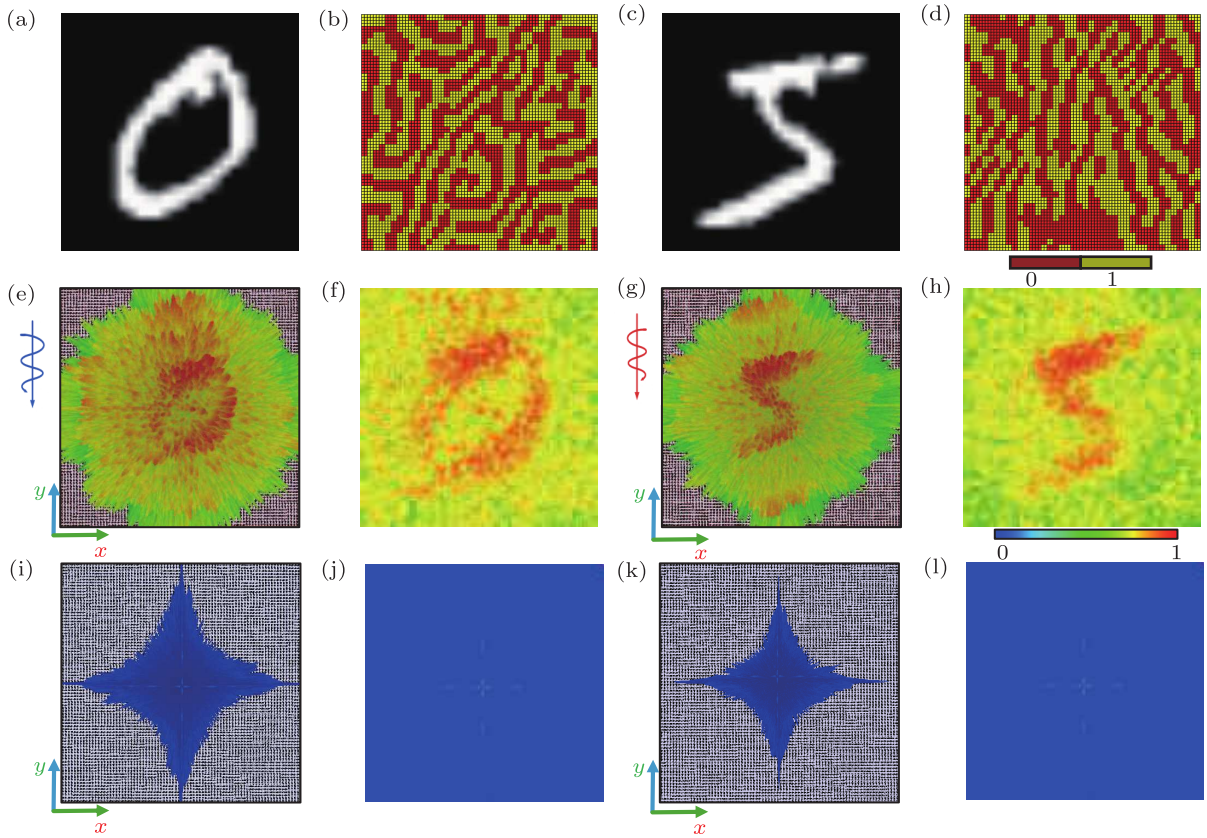


Fig. 8. Target images, extracted phases, and reconstructed holographic patterns of the DSM metasurface. (a) and (c) Target images '0' and '5'; (b) and (d) corresponding phase distributions extracted using the GS algorithm. Under the on state (DSM Fermi level $E_F = 0.5$ eV): (e) 3D far-field and (f) 2D far-field images of digital '0' reconstructed under LCP incidence; (g) 3D far-field and (h) 2D far-field images of digital '5' reconstructed under RCP incidence. Under the off state (DSM Fermi level $E_F = 0.022$ eV): the LCP and RCP channel reflections are suppressed, resulting in the disappearance of imaging; (i) 3D far-field and (j) 2D far-field images of digital '0'; (k) 3D far-field and (l) 2D far-field images of digital '5'.

Utilizing the extracted phase information, we selected matching structural units to construct a 40×40 metasurface array, where each structural unit comprises 2×2 sub-units to mitigate coupling interference between units. When the DSM Fermi level is set to 0.5 eV, the metasurface successfully reconstructs a hologram of the digital '0' under LCP incidence and a hologram of the digital '5' under RCP incidence. Conversely, when the DSM Fermi level is lowered to 0.022 eV, the metasurface exhibits nearly no reflection, rendering both LCP and RCP channels incapable of forming effective pat-

terns, thereby demonstrating excellent optical 'off' characteristics.

The effects of the metasurface under LCP incidence are depicted in Figs. 8(e)–8(h), while those under RCP incidence are shown in Figs. 8(i)–8(l). These results indicate that, aided by the coordinated encoding of ETP and PB phases, along with the electrical tunability of the DSM Fermi level, real-time switching and decoupling of dual-channel holographic patterns can be accomplished on a single device, thereby presenting a novel design paradigm for reconfigurable terahertz information display and multi-mode multiplexing.

3.4. Grayscale imaging of LCP absorbance based on EPs

Additionally, we observed that the structures located at three different EPs exhibited significant differences in absorption rates under both LCP and RCP channels, particularly after rotating the structures at specific angles, which further accentuated these differences.

Leveraging this characteristic, we developed a grayscale imaging method for the LCP channel based on reflection regulation, enabling controllable display and concealment of images. For demonstration, we selected an image of a 'little grey dog' composed of 80×80 pixels, as illustrated in Fig. 9(c). The pixel values were extracted and normalized into four distinct intensity levels, represented as 0, 1, 2, and 3. When the DSM Fermi level is set to 0.5 eV, the reflectivity of each unit structure under LCP incidence is calculated using

$$A_{\mathrm{LCP}} = 1 - |R_{-+}|^2 - |R_{++}|^2 .$$

We then selected four metasurface units with varying reflectivity levels corresponding to the four grayscale intensity levels of the image, as illustrated in Figs. 9(a) and 9(b). The structural parameters of the four designed units are as follows: $(L_1, L_3, \theta) = (4.23\ \mu\mathrm{m}, 8.252\ \mu\mathrm{m}, 90^\circ)$, $(4.23\ \mu\mathrm{m}, 8.252\ \mu\mathrm{m}, 154^\circ)$, $(1.94\ \mu\mathrm{m}, 7.794\ \mu\mathrm{m}, 226^\circ)$, and $(4.035\ \mu\mathrm{m}, 9.465\ \mu\mathrm{m}, 106^\circ)$, corresponding to structures 1, 2, 3, and 4, respectively. The reflectivities of these units to LCP correspond to image intensities of 3, 2, 1, and 0.

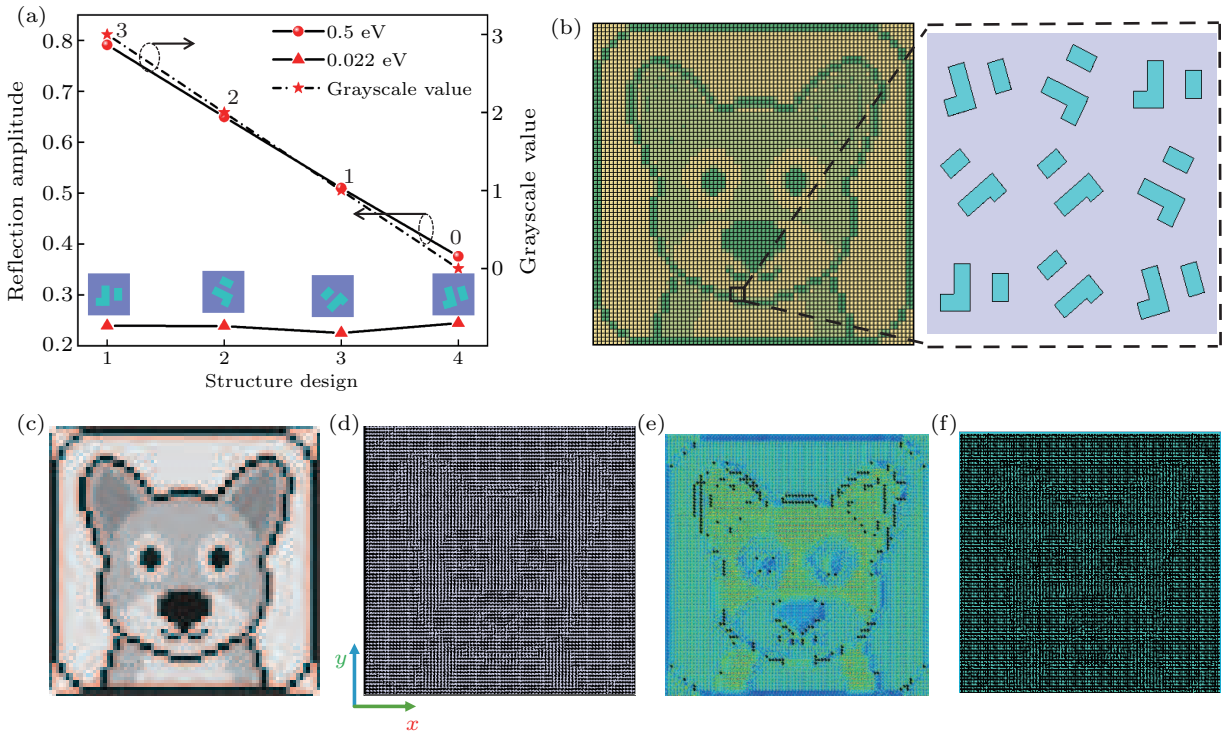


Fig. 9. Grayscale imaging control based on EP-induced absorption differences under LCP incidence at a frequency of 6.597 THz. (a) Comparison of reflection amplitudes of four structural units at Fermi energy levels $E_{\mathrm{F}} = 0.5$ eV and $E_{\mathrm{F}} = 0.022$ eV, along with the corresponding grayscale intensities, demonstrating their ability to distinguish LCP absorption characteristics. (b) Grayscale extraction of the target image and corresponding metasurface arrangement at the local position. (c) Original image of the 'little grey dog'. (d) Global arrangement of the metasurface based on the grayscale mapping of the image. (e) Under the 'on state' ($E_{\mathrm{F}} = 0.5$ eV), each structural unit exhibits contrast due to different absorption rates, achieving clear image reconstruction. (f) Under the 'off state' ($E_{\mathrm{F}} = 0.022$ eV), the absorption rates of all structural units become uniform, the reflected image disappears, and the system enters an effectively invisible state.

When the DSM Fermi level is set to 0.022 eV, the reflectivity of all four metasurface units to LCP becomes nearly identical. By arranging these units according to the grayscale mapping of the target image to form a metasurface, and illuminating it with LCP at a frequency of 6.597 THz, the designed structure can clearly reconstruct the image of the 'little grey dog' at $E_{\mathrm{F}} = 0.5$ eV, as shown in Figs. 9(c) and 9(d). Conversely, when the Fermi level is lowered to 0.022 eV, the reflection of the image disappears due to uniform unit reflectivity, resulting in the entire system entering the 'off' state, as

depicted in Fig. 9(e).

This method effectively demonstrates the feasibility of utilizing EPs to control absorption for programmable grayscale imaging, paving the way for advancements in grayscale display and dynamic dimming of terahertz metasurfaces.

4. Conclusion

In this study, we designed an adjustable ETP coding metasurface based on three-dimensional DSM to overcome the technical bottleneck associated with dynamic multifunctional control of terahertz metasurfaces. We systematically elucidated the theoretical foundation, device design, and experimental validation of its multi-dimensional dynamic control within the terahertz band. Coupled-mode theory was employed to explain the generation of three EPs and the conservation law of topological charge on the PT-symmetric metasurface. Furthermore, orthogonal control of the phases of left-handed and right-handed circularly polarized channels was achieved through the integration of the PB phase.

By tuning the DSM Fermi level, we successfully demonstrated reversible switching of vortex beams, dual-channel wavefront multiplexing, real-time holographic switching, and near-field grayscale imaging based on absorption differences. In dynamic light-field modulation, the realized 'switching' function transcends a mere transition between high and low signal levels; it embodies a coordinated transition of both phase and amplitude near the EP. This capability enables the device to rapidly reconfigure light-field modes, polarization states, and spatial distributions on a single structural platform. The coherence-switching mechanism, driven by Fermi-level tuning, highlights the distinctive physical advantages of the non-Hermitian exceptional topological phase in the terahertz regime. Notably, it leverages the robustness of the topological phase to ensure stability and high contrast throughout the switching process.

These results underscore the unique advantages of co-designing non-Hermitian topological optics with tunable quantum materials, enhancing the versatility, integration, and response speed of devices, and providing a novel paradigm for high-capacity terahertz communications, programmable near-field/far-field imaging, and multi-mode light-field processing. In terms of applications, this switching mechanism can be extensively utilized in dynamic channel encryption for terahertz secure communications, rapid mode switching in frequency-division and mode-division multiplexing systems, and programmable appearance and disappearance as well as adaptive focusing in terahertz imaging and sensing. These applications significantly enhance system flexibility and increase information-carrying capacity.

The DSM-ETP metasurface not only achieves full-dimensional control of phase, amplitude, and polarization within a single frequency band but also facilitates working/off state conversion on a nanosecond scale through Fermi-level manipulation, demonstrating excellent reconfigurability and system compatibility. This study establishes a robust experimental foundation for the application of non-Hermitian topological phases in subwavelength devices and injects new vitality into application scenarios such as secure communications, intelligent sensing, and dynamic displays in the terahertz-millimeter wave domain.

Acknowledgments

This work was supported by the National Natural Science Foundation of China (Grant No. 62375158), the Qingdao Natural Science Foundation (Grant No. 25-1-1-153-zyyd-jch), and the Development Plan of Youth Innovation Team in Colleges and Universities of Shandong Province (Grant No. 2022KJ216).

References

[1] Zheludev N I and Kivshar Y S 2012 *Nat. Mater.* **11** 917
[2] Chen H T, Taylor A J and Yu N 2016 *Rep. Prog. Phys.* **79** 076401
[3] Yu N, Genevet P, Kats M A, Aieta F, Tetienne J P, Capasso F and Gaburro Z 2011 *Science* **334** 333
[4] Glybovski S B, Tretyakov S A, Belov P A, Kivshar Y S and Simovski C R 2016 *Phys. Rep.* **634** 1
[5] Li J H, Xiong H T, Kong D Y, Zhao W P, Liu S J, Quan B G and Wu X J 2024 *Chin. Phys. Lett.* **41** 124201
[6] Li Z, Jiang C, Wang K, Liu M, Li C, Tian C, Zhang H and Zhang Y 2023 *Results Phys.* **46** 106323
[7] Zhang Y, Jiang C, Li Z, Sang X, Wang J, Sun X, Zhao S, Lu B, Liu M and Zhang H 2024 *Results Phys.* **56** 107287
[8] Rao S J M, Sarkar R, Kumar G and Roy Chowdhury D 2019 *OSA Continuum* **2** 603
[9] Chu Z, Cai X, Zhu R, Liu T, Sun H, Li T, Jia Y, Han Y, Qu S and Wang J 2024 *OEA* **7** 240045
[10] Landy N I, Sajuyigbe S, Mock J J, Smith D R and Padilla W J 2008 *Phys. Rev. Lett.* **100** 207402
[11] Ren B, Feng Y, Tang S, Wang L, Jiang H and Jiang Y 2021 *Opt. Express* **29** 17258
[12] Cui T J, Qi M Q, Wan X, Zhao J and Cheng Q 2014 *Light. Sci. Appl.* **3** e218
[13] Liu T, Meng Y, Wang J, Ma H, Zhu R, Liu C, Li W, Chu Z, Sui S, Qiu T, Tang W and Qu S 2023 *Photon. Res.* **11** 1047
[14] Liu W, Dai J Y, Zhang Y M, Sun M K, Zhang L, Li Y, He H J, Cui T J and Cheng Q 2024 *Laser & Photon. Rev.* **18** 2400049
[15] Zhang J, Li P, Cheung R C C, Wong A M H and Li J 2023 *Adv. Photon.* **5** 036001
[16] Zhang L, Chen X Q, Liu S, Zhang Q, Zhao J, Dai J Y, Bai G D, Wan X, Cheng Q, Castaldi G, Galdi V and Cui T J 2018 *Nat. Commun.* **9** 4334
[17] Zhang N, Chen K, Zheng Y, Hu Q, Qu K, Zhao J, Wang J and Feng Y 2020 *IEEE J. Emerg. Sel. Topics Circuits Syst.* **10** 20
[18] Ding G, Chen K, Luo X, Zhao J, Jiang T and Feng Y 2019 *Phys. Rev. Appl.* **11** 044043
[19] Yu S, Guan D, Gu Z, Shi J, Liu Z and Liu Y 2025 *IEEE Trans. Aerosp. Electron. Syst.* **61** 121
[20] Feng Q, Kong X, Shan M, Lin Y, Li L and Cui T J 2022 *Phys. Rev. Appl.* **17** 034017
[21] Li J S and Chen Y 2023 *Chin. Phys. B* **32** 124204
[22] Wu R Y, Shi C B, Liu S, Wu W and Cui T J 2018 *Adv. Opt. Mater.* **6** 1701236
[23] Liu S, Cui T J, Zhang L, Xu Q, Wang Q, Wan X, Gu J Q, Tang W X, Qing Qi M, Han J G, Zhang W L, Zhou X Y and Cheng Q 2016 *Adv. Sci.* **3** 1600156
[24] Yan X, Huai F, Zhang Y, Lv K, Liang L, Li Z, Wang Z, Yao H, Hu X, Li Y, Wang M, Liu Y, Ma S, Tian H, Wang X and Wu J 2025 *Opt. Express* **33** 7579

[25] Xu P, Liu H, Li R, Zhang K and Li L 2022 *IEEE Trans. Antennas Propagat.* **70** 10678

[26] Song Q, Odeh M, Zúñiga-Pérez J, Kanté B and Genevet P 2021 *Science* **373** 1133

[27] Lawrence M, Xu N, Zhang X, Cong L, Han J, Zhang W and Zhang S 2014 *Phys. Rev. Lett.* **113** 093901

[28] Fu P, Du S, Lan W, Hu L, Wu Y, Li Z, Huang X, Guo Y, Zhu W, Li J, Liu B and Gu C 2023 *Physics* **6** 254

[29] Zhang Y, Li Z, Jiang C, Wang K, Lv X, Sang X, Wang J, Liu M and Zhang H 2023 *Appl. Phys. Express* **16** 092002

[30] Yang Z, Huang P S, Lin Y T, Qin H, Zúñiga-Pérez J, Shi Y, Wang Z, Cheng X, Tang M C, Han S, Kanté B, Li B, Wu P C, Genevet P and Song Q 2024 *Nat. Commun.* **15** 232

[31] Yang Z, Huang P S, Lin Y T, Qin H, Chen J, Han S, Huang W, Deng Z L, Li B, Zúñiga-Pérez J, Genevet P, Wu P C and Song Q 2024 *Nano Lett.* **24** 844

[32] Li Y, Wan S, Deng S, Deng Z, Lv B, Guan C, Yang J, Bogdanov A, Belov P and Shi J 2024 *Photon. Res.* **12** 534

[33] Lang Y, Xu Q, Xu G, Zhang X, Li Q and Han J 2025 *Laser & Photon. Rev.* **19** 2401281

[34] Kim J, Jeong M, Jung C, Seong J and Rho J 2025 *Adv. Funct. Mater.* **35** 2501916

[35] Álvarez-Sanchis J A, Vidal B, Tretyakov S A and Díaz-Rubio A 2023 *Phys. Rev. Appl.* **19** 014009

[36] Nemati A, Wang Q, Hong M and Teng J 2018 *Opto-Electron. Adv.* **1** 18000901

[37] Folland T G, Fali A, White S T, Matson J R, Liu S, Aghamiri N A, Edgar J H, Haglund R F, Abate Y and Caldwell J D 2018 *Nat. Commun.* **9** 4371

[38] Zhou R, Ullah K, Hussain N, Fadhali M M, Yang S, Lin Q, Zubair M and Iqbal M F 2022 *Adv. Photon. Nexus* **1** 024001

[39] Yuan H X, Li J X, Ma Q J, Tian H S, Ye Y Y, Luo W X, Wu X H and Jiang L Y 2024 *Chin. Phys. B* **33** 034213

[40] Gao W, Shu J, Qiu C and Xu Q 2012 *ACS Nano* **6** 7806

[41] Lan F, Wang L, Zeng H, Liang S, Song T, Liu W, Mazumder P, Yang Z, Zhang Y and Mittleman D M 2023 *Light Sci. Appl.* **12** 191

[42] Ermolaev G, Voronin K, Baranov D G, Kravets V, Tselikov G, Stebunov Y, Yakubovsky D, Novikov S, Vyshnevyy A, Mazitov A, Kruglov I, Zhukov S, Romanov R, Markeev A M, Arsenin A, Novoselov K S, Grigorenko A N and Volkov V 2022 *Nat. Commun.* **13** 2049

[43] Zhong M and Li J 2022 *Opt. Commun.* **511** 127997

[44] Hu Y, Chen S N, Shi Y, Liu X and Wang J Y 2024 *Adv. Mater. Technol.* **9** 2302164